ELSEVIER

Earth and Planetary Science Letters 197 (2002) 117–131

EPSL

www.elsevier.com/locate/epsl

Peridotite melting and mineral–melt partitioning of major and minor elements at 22–24.5 GPa

Reidar G. Trønnes [a,*], Daniel J. Frost [b]

[a] *Nordic Volcanological Institute, University of Iceland, Grensásvegur 50, IS-108 Reykjavik, Iceland*
[b] *Bayerisches Geoinstitut, Universität Bayreuth, D-95447 Bayreuth, Germany*

Received 2 July 2001; received in revised form 2 November 2001; accepted 2 January 2002

Abstract

Melting experiments at 2100–2400°C and 22–24.5 GPa to determine the liquidus to solidus phase relations and element partitioning coefficients were performed on different peridotite compositions: a pyrolite model and a KLB-1 composition. These starting materials, prepared as oxide mixes, were contained in Re capsules. The experiments were carried out using cubic-octahedral multianvil presses with 10/4 mm (octahedral edge length/anvil truncation edge length) and 18/8 mm pressure cell configurations with $LaCrO_3$ heaters and axially inserted W–Re thermocouples. The 18/8 mm configuration with a stepped heater was developed in order to reduce the experimental thermal gradients. Some of the experiments were performed with Re-rod sample containers with two parallel chambers, allowing two different compositions to be run at identical conditions. Within experimental uncertainties, the melting relations of the KLB-1 and pyrolite compositions are identical in the 22–24.5 GPa range. Ringwoodite does not occur either in the melting range or just below the solidus, even at 22 GPa. Garnet (ga) and ferropericlase (fp) are the first liquidus phases at 22–23 GPa and at 24–24.5 GPa, respectively. The crystallization sequence is ga-fp-Ca-perovskite (cpv) at 22 GPa, ga-fp-perovskite(pv)-cpv at 23 GPa, and fp-pv-ga-cpv at 24–24.5 GPa. Major element distribution between the different phases implies that the solidus is approximately coincident with the appearance of cpv. The major element mineral–melt partitioning shows only minor variations with pressure in the investigated range. The mineral–melt $K_D(Fe/Mg) = (Fe/Mg)_{mineral}/(Fe/Mg)_{melt}$ decreases from 0.64 at 22–23 GPa to 0.62 at 24.5 GPa for ferropericlase and is below 0.46 for garnet and perovskite. The $K_D(Si/Mg)$ for garnet and perovskite decrease slightly from 1.34 at 22 GPa to 1.16 at 24.5 GPa. The Ca/Al ratio is elevated in the melt phase with mineral–melt $K_D(Ca/Al)$ for garnet and perovskite below 0.4. The partitioning coefficients indicate that partial melting or fractional crystallization in the transition zone and the uppermost part of the lower mantle will produce melts with elevated ratios of Fe/Mg and Ca/Al. The partitioning of minor elements like Ti, Cr, Ni and Na is strongly dependent on the proportions of the fractionating phases.

Keywords: peridotites; high pressure; melting; perovskite; garnet group; periclase

* Corresponding author. Tel.: +354-525-4496; Fax: +354-562-9767.
E-mail address: rgt@norvol.hi.is (R.G. Trønnes).

0012-821X/02/$ – see front matter
PII: S0012-821X(02)00466-1

1. Introduction

Partial melting of mantle peridotite at pressures below 5 GPa produces the vast majority of mafic magma types seen at the Earth's surface. At various times during the early history of the Earth, however, peridotite melting may have occurred at much higher pressures, corresponding to the transition zone and the upper part of the lower mantle. Impacts of giant planetesimals during the later stages of the accretion of the Earth may have resulted in partial or complete melting of the mantle [1]. Fractional crystallization of such a magma ocean may have produced an early stratification of the mantle, although convective stirring may have greatly reduced such a layering [2]. Hotter plumes rising through the Archean mantle, however, may also have experienced initial melting in the upper part of the lower mantle [3,4].

The lack of precise and reliable element partitioning coefficients between melt and residual minerals stable in the lower mantle and the transition zone has caused uncertainties and debate over the possible consequences of fractionation processes related to the crystallization of a magma ocean and to melt separation from hot plumes (e.g. [5,6]). A knowledge of the melting phase relations and element partitioning expected during melting of peridotite at high pressure is therefore of great interest. In addition, the study of equilibrium partitioning between phases at high pressure is often hindered by the difficulty in attaining equilibrium at plausible mantle temperatures. During melting, however, rapid transport in the liquid aids the attainment of equilibrium and crystal-chemical influences over element partitioning between solids and between solid and liquid phases can be studied.

Although several studies have examined melting relations of peridotitic and chondritic compositions and mineral–melt partitioning at transition zone and lower mantle conditions (e.g. [7–14]), the solidus to liquidus phase relations above 22 GPa are still not well established. The mineral–melt partitioning of major and trace elements above 20 GPa, including the effect of pressure, is also uncertain. Here we report results of melting experiments performed on mantle peridotite compositions between 22 and 24.5 GPa. These new data were collected with specific attention paid to the minimization of thermal gradients at high pressure. A selection of 20 trace elements doped at the 60–800 ppm level (in total 0.53 wt%) were added to some of the starting powders in order to extract trace element partitioning data, which will be reported separately.

2. Experimental technique

Table 1 lists the experimental conditions and observed phase relation. The major element compositions of the KLB-1 and pyrolite starting compositions are given in Table 2. The starting compositions were produced from reagent grade oxides and carbonates, which were ground together in alcohol and decarbonated at 1000°C in air. A selection of 20 trace elements with an oxide total of 0.61 wt% were added to the pyrolite composition using AAS standard solutions. The powdered mixes were subsequently devolatilized at 400°C in air. Cold pressed pellets of starting powders were reduced in a CO_2–CO gas mix furnace at 1200°C and at an f_{O_2} of two log units below the fayalite–magnetite–quartz oxygen buffer. The recovered pellets were reground to a grain size of 5–10 μm.

In order to minimize thermal gradients during the experiments, sample capsules were kept as short as possible. Re foil capsules 1 mm long were used and in addition multichamber capsules were fabricated from 0.6 mm long Re rods by spark-eroding the sample holes. Two sample chambers, 0.3 mm in diameter, in each rod allowed two starting materials to be run in a single experiment.

Experiments were conducted in a 1200 ton split sphere multianvil apparatus using a 10 mm edge length Cr_2O_3-doped MgO octahedron and 32 mm WC cubes with 4 mm edge length truncations. In order to investigate the melting relations in an environment of more reduced thermal gradients, some of the experiments were performed with larger pressure cells (18 mm octahedral edge lengths) in a 5000 ton split cylinder multianvil press, using 54 mm Toshiba F grade cubes with

8 mm edge length corner truncations. In the latter configuration, a pressure of 23 GPa was reached by press loads of 2000 tons. The larger 18 mm octahedra provide space for narrow and stepped $LaCrO_3$ furnaces that resulted in thermal gradients (determined by two-pyroxene thermometry), on the order of 50°C/mm at 1400°C, as opposed to gradients of more than 100°C/mm in a 10 mm octahedron at the same temperature.

The high-temperature pressure calibrations were performed at 1600°C and 2000°C. The calibration curves are based on the following transitions in the compositions $MgSiO_3$ and Mg_2SiO_4: forsterite–wadsleyite, wadsleyite–ringwoodite and ilmenite–perovskite [15,16], with reference to the Jamieson et al. [17] equation of state for gold. An additional calibration check point at 26 GPa was provided by the compositions of coexisting garnet and perovskite in the enstatite–pyrope system [18]. The pressure calibration has been adjusted relative to preliminary reports [19,20]. Using the recently modified pressure scale [21,22] based on the Anderson et al. [23] equation of state for gold, our pressure values must be lowered by about 2 GPa. The current uncertainties [24,25] and the advantage of direct comparison with the pressure

Table 1
List of experiments

Run number	Starting material	p (GPa)	Nominal T (°C)	Duration (min)	Mineral assemblage (crystallization sequence)
2377	py	22	2150	20	subsolidus: ga-fp-cpv
2373	py*	22	2160	20	L-ga-fp-cpv
2374	py	22	2160	20	L-ga-fp-cpv
2376	py	22	2250	20	L-ga-fp
Z121	py	23	2140	20	subsolidus: ga-fp-pv-cpv
Z126	py	23	2160	15	near solidus: iL-ga-fp-pv-cpv
Z119	py	23	2200	10	L-ga-fp
2392	KLB	24	2180	5	L-fp-pv-ga-cpv
2381	py	24	2200	10	L-fp-pv-ga-cpv
2389	py+Fe	24	2240	8	L-fp-ga-pv-cpv
2383	py	24	2250	10	L-fp-pv (+quench-ga)
2387	KLB	24	2310	10	L-fp-pv-ga-cpv
2384	py	24	2340	5	above liquidus
2462	py	24.5	–	15	subsolidus: fp-pv-ga-cpv
	KLB				subsolidus: fp-pv-ga-cpv
2430	py	24.5	2130	10	subsolidus: fp-pv-ga-cpv
	KLB				subsolidus: fp-pv-ga-cpv
2465	py	24.5	2230	40	near solidus: iL-fp-pv-ga-cpv
	KLB				near solidus: iL-fp-pv-ga-cpv
2432	py	24.5	2270	10	L-fp-pv (+quench-ga)
	KLB				L-fp-pv-ga
2438	py	24.5	2270	20	L-fp-pv-ga
	KLB				L-fp-pv-ga
2428	py	24.5	–	3	above liquidus
	KLB				L-fp
2425	py	24.5	2400	2	L-fp
	KLB				L-fp

18–8 mm assemblies were used for experiments at 23 GPa, 10–4 mm assemblies at all other pressures. Sample capsules: Re-foil, except for experiments 2276 and 2383 (Re-rod capsules with one sample chamber) and all 24.5 GPa experiments (Re-rod capsules with two sample chambers). The nominal temperature was recorded by the thermocouple during heating. After arrival at run temperature, the experiments were kept at constant electrical power output. Temperatures are not given for two experiments with no thermocouple control during heating.

Starting materials: py, pyrolite [29] with added trace elements; py*, pyrolite without trace elements; py+Fe, pyrolite with trace elements and an extra addition of 1% Fe metal; KLB, KLB-1 peridotite [30] without trace elements. Mineral assemblages: L, melt; iL, inferred interstitial melt; ga, majoritic garnet; fp, ferropericlase; pv, MgSi-perovskite; cpv, CaSi-perovskite.

Table 2
Composition of starting materials, quenched melts and coexisting liquidus minerals

		SiO_2	Al_2O_3	TiO_2	Cr_2O_3	NiO	FeO	MnO	MgO	CaO	Na_2O	Σ_{ox}	Mg#		
Pyrolite		45.0	4.45	0.20	0.04	0.25	8.05	0.14	37.8	3.55	0.36	99.84	89.3		
KLB-1		44.5	3.59	0.16	0.31	0.25	8.10	0.12	39.2	3.44	0.30	99.97	89.6		
qm	22	45.9	4.58	0.16	0.08	0.21	8.26	0.14	37.3	3.21	na	99.84	88.7		
	23	46.3	3.48	0.24	0.03	0.22	8.57	0.16	35.4	4.03	na	98.43	88.0		
	24	46.4	4.07	0.17	0.28	0.23	8.61	0.16	36.0	3.33	na	99.25	88.2		
	24.5	46.0	4.03	0.14	0.31	0.19	8.43	0.17	35.5	4.42	0.3	99.49	88.3		
fp	22	0.24	1.57	–	0.08	0.91	11.9	0.09	84.2	0.05	0.15	99.19	92.7		
	23	0.23	1.24	0.02	0.04	0.89	13.2	0.11	84.3	0.05	na	100.1	91.9		
	24	0.16	1.33	0.02	0.39	0.95	12.7	0.10	84.0	0.16	na	99.81	92.2		
	24.5	0.11	1.30	–	0.43	0.84	12.6	0.14	84.3	0.05	0.19	99.96	92.3		
ga	22	53.4	9.92	0.04	0.08	0.06	2.55	0.05	32.6	1.82	0.10	100.6	95.8		
	23	54.2	7.17	0.08	0.06	0.02	3.24	0.12	32.1	2.81	na	99.80	94.6		
	24	53.1	9.65	0.11	0.31	0.09	3.36	0.12	31.4	2.62	na	100.8	94.3		
pv	24	55.8	3.96	0.23	0.27	0.05	3.73	0.08	35.7	1.00	na	100.8	94.5		
	24.5	54.4	3.73	0.19	0.23	0.05	3.98	0.06	36.1	0.86	0.01	99.61	94.2		
1σ	q-m	0.98	0.28	0.03	0.04	0.04	0.60	0.02	1.20	0.38	0.06				
1σ	mw	0.07	0.05	–	0.05	0.09	0.26	0.03	0.51	0.02	0.04				
1σ	ga	0.63	0.67	0.02	0.05	0.02	0.23	0.02	0.76	0.26	0.06				
1σ	pv	0.52	0.25	0.05	0.04	0.03	0.24	0.02	0.50	0.13	0.02				
		Si	Al	Ti	Cr	Ni	Fe	Mn	Mg	Ca	Na	$\Sigma_{cat.prop}$	ST	AC	NN
fp	22	21	158	–	5	63	854	7	10 784	5	26	11 897			
	23	20	125	1	3	61	944	8	10 749	5	na	11 915			
	24	14	135	1	26	65	912	7	10 729	14	na	11 904			
	24.5	9	132	–	29	58	901	10	10 766	5	31	11 910			
ga	22	3 614	792	2	4	3	144	3	3 292	132	14	8 000	3 616	796	3 574
	23	3 717	580	4	3	1	186	7	3 282	206	na	7 986	3 721	583	3 682
	24	3 615	774	5	17	5	191	7	3 181	191	na	7 986	3 620	791	3 575
pv	24	3 790	317	12	14	3	212	4	3 609	73	na	8 034	3 802	331	3 901
	24.5	3 749	303	10	12	3	230	4	3 709	63	2	8 085	3 750	315	4 011

Oxides in wt% and cations normalized to a total charge of 24 000 (12 000 oxygen atoms). The average compositions listed here are average values of the liquidus phases in one to seven different experimental charges. In each of the charges the liquidus phase compositions are the averages of three to 15 spot analyses, and the 1σ values refer to the average deviations from these mean values. The starting compositions of pyrolite [29] and KLB-1 [30] were prepared by combining oxides and carbonates before heating at 1200°C at an oxygen fugacity two log units below the fayalite–magnetite–quartz oxygen buffer to convert all of the ferric iron to ferrous iron. The pyrolite composition used here has about 10 times lower Cr content than that of [29]. In the averaging procedure used for the quenched melt and mineral analyses, only the Cr contents of the KLB-1 composition experiments are used, except for those pressures (22 and 23 GPa) where only the pyrolite composition is available. The numbers 22, 23, 24, and 24.5 denote pressure (in GPa). qm, quenched melt; fp, ferropericlase; pv, MgSi-perovskite; ga, majoritic garnet; na, not analyzed; Mg = 100*Mg/(Mg+Fe), where Fe is total iron; ST = Si+Ti; CA = Al+Cr; NN = Ni+Fe+Mn+Mg+Ca+Na.

values of published phase equilibrium studies on peridotite compositions make the use of the old pressure scale [15–17] our natural choice. The temperature was measured using WRe3/WRe25 thermocouples with no pressure correction of the thermocouple EMF.

The individual components of the pressure assembly, including octahedra, ZrO_2 insulating sleeves, MgO spacers and the $LaCrO_3$ heater parts, were fired at 1000°C for 1–2 h. After complete assembly the octahedra with capsules were kept at 250°C in a vacuum oven for at least 10 h before an experiment. Experiments were performed by increasing the pressure over a duration of 4 h, followed by slow heating to 1400°C (250°C/min). The temperature was kept at 1400°C for 20 min, before rapid heating to the run temperature (500°C/min). The nearly linear

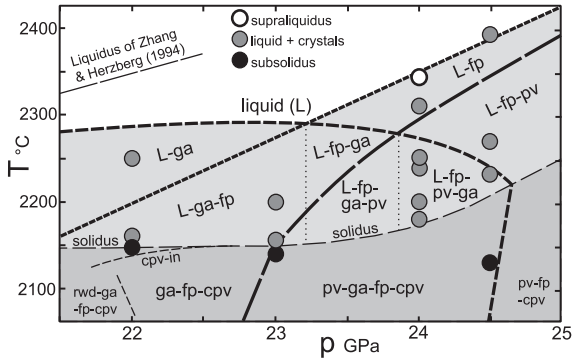

Fig. 1. Phase relations of pyrolite and KLB-1. Within the experimental uncertainties, the two investigated compositions have identical phase relations. The bold lines with short, intermediate and long stipples limit the fields of ferropericlase, garnet, and perovskite, respectively. Abbreviations as in Tables 1 and 2 (rwd, ringwoodite). The exact location of the solidus is problematic, because a small fraction of interstitial melt is not easily observable. The major element variation between coexisting phases and the bulk composition indicates that the appearance of Ca-perovskite occurs near the solidus. The cpv-in curve seems to be slightly below the solidus at 22 GPa and coincide with the solidus at higher pressures. At 22 GPa our solidus determination is identical to that of Zhang and Herzberg [8] and Herzberg et al. [27]. The liquidus of Zhang and Herzberg [8] up to 22.5 GPa is shown about 50–75°C above our inferred liquidus temperature. The approximate locations and sense of slopes (negative and positive, respectively) of the subsolidus ringwoodite-out and garnet-out reaction boundaries are partly based on [26,28] but drawn according to our experimental constraints. The positive slope of the subsolidus perovskite-in boundary is drawn according to Hirose [28].

relation observed between electrical power and temperature during heating indicates that the power output is a reliable guide to the temperature. At run temperatures of 2100–2400°C, the thermocouple EMF often drifted slowly in spite of a constant power output. Therefore, the experiments were run manually at constant power output as soon as the run temperature was reached. This resulted in far more consistent melting observations than when the thermocouple temperature was followed throughout the heating duration.

The thermal gradients within the sample capsules vary according to the exact location relative to the midpoint of the $LaCrO_3$ furnace. The observed distance between the inferred liquidus and solidus positions within some of the sample capsules in comparison with the results of this melting study and previous studies (e.g. [8]) indicate that the thermal gradients at 2100–2400°C are considerably larger than those measured by two-pyroxene thermometry at 1400°C, probably on the order of 200°C/mm.

The boundary between 100% quenched melt and equilibrium crystals with interstitial melt is loosely referred to as the liquidus interphase. The isotherm corresponding to this boundary, however, is not necessarily identical with the liquidus temperature, if some liquid–solid separation has occurred along the thermal gradient. Liquid–solid separation, however, is inferred to be unimportant because the quenched melt areas have fairly constant compositions similar to the bulk starting compositions (see below). The solidus cannot be observed directly in these experiments. Chemical mass balance constraints involving mineral and melt compositions, however, indicate that the appearance of Ca-perovskite is nearly coincident with the solidus in the investigated pressure range.

3. Analytical method

Recovered capsules were mounted in epoxy resin for analysis with Raman spectroscopy and electron microprobe. Two samples were also made into doubly polished thin sections for Fourier transform infrared (FTIR) spectroscopy and Mössbauer spectroscopy at the Bayerisches Geoinstitut. Electron microprobe analyses were performed in Bayreuth using a Cameca SX-50, at the Mineralogical-Geological Museum in Oslo with a Cameca Camebax Microbeam instrument and at the University of Bristol with a Jeol-8600 Superprobe. The instruments operated at an accelerating voltage of 15 kV with a beam current of 15–20 nA. The raw data were corrected by a combination of PAP and ZAF correction programs. Synthetic silicates and oxides were used as standards and the standards varied between the various microprobe locations. The minerals were mostly analyzed with a focused beam. Perovskite, which structurally decomposed under the electron beam, was analyzed both with a focused and with

a defocused beam of 5 μm diameter. No compositional difference between focused and defocused beam analyses were found, in line with the observations of Wood [26]. The damage that occurs to perovskite during analysis does not therefore seem to affect the determined composition. The quenched melt areas were analyzed partly with a raster mode of analysis covering areas of 400–700 μm^2 and partly by systematic and dense point transects using a defocused beam with 10 μm diameter. No systematic compositional variations were observed between the analytical data generated by the different methods and between the different laboratories.

The estimated precision and accuracy for analyses of quenched melt and different minerals, given in Table 2, are based on repeated analyses of the experimental phases and standards (10–30 analyses of each phase). Although the spatial variation of quenched melt compositions within the all-melt portions of the experimental charges are generally within the precision range, the reported melt analyses are from areas close to the liquidus. Some of the majoritic garnet crystals between the liquidus and the solidus are slightly zoned. In these cases the cores have higher Fe/Mg ratios than the rims, and they represent incompletely equilibrated subsolidus compositions formed during heating toward the run temperature. In the case of zoned crystals, the spot analyses were performed on the rims in equilibrium with the adjacent melt.

4. Results

4.1. Phase relations

The two peridotite compositions investigated have identical phase relations within the experimental resolution of this study, and there is no resolvable effect of the addition of a total of 0.55 wt% trace elements. The phase relations for these peridotite compositions at pressures of 22–24.5 GPa are shown in Fig. 1, and backscatter electron (BSE) images of representative liquidus assemblages at pressures of 23, 24 and 24.5 GPa are shown in Fig. 2. The thermal gradients across the sample capsules produce isobaric sections, covering a range of temperatures. Some of the run products cover the entire or part of liquidus to solidus range, whereas others are entirely subsolidus or supraliquidus (Table 1).

The Fe–Mg-dominated oxide phases, referred to as ferropericlase, have atomic Mg/(Mg+Fe) ratios well above 0.8, even in the subsolidus. The liquidus or near-liquidus ferropericlase has Mg/(Mg+Fe) ratio of more than 0.9 in the entire pressure range.

Below about 23.2 GPa majoritic garnet (ga) is the liquidus phase followed by ferropericlase (fp). At higher pressures ferropericlase is the liquidus phase, followed by garnet and then perovskite (MgSi-perovskite, pv) and at 24 GPa the second crystallizing phase is perovskite followed by garnet. The crystallization of CaSi-perovskite (cpv) occurs slightly below the solidus at 22 GPa, but is nearly coincident with the solidus at higher pressures. Garnet becomes a near-solidus phase at 24.5 GPa. Recent studies of the subsolidus phase relations of peridotite compositions indicate that the gradual dissolution of garnet into perovskite with increasing pressure is completed at about 24.5 GPa at a temperature of 2100°C [26,28].

The crystallization sequences at various pressures are illustrated in Fig. 2. The BSE images demonstrate the lower thermal gradients, leading

→

Fig. 2. BSE images of four experimental products. Abbreviations as in Tables 1 and 2. The widths of the five images in μm are 745 (A), 238 (B), 184 (C), 189 (D) and 1080 (E) and 154 (F). Note the lower thermal gradient in exp. Z119 (A,B, 18–8 mm assembly) compared to exp. 2387 and 2432 (C,D, 10–4 mm assemblies). The crystallization sequences are ga-fp (A,B), fp-pv (C,D) and only fp (E,F). Some of the large quench perovskite crystals in C and D have arrowhead-like terminations. The small and rounded fragments (2–5 μm in diameter, especially in D) of high BSE brightness are Re fragments immersed in the sample powder during the packing of the powder in the capsules (see also [11]). A,B: 23 GPa, Z119; C: 24 GPa, exp. 2387, KLB-1; D: 24.5 GPa, exp. 2432, KLB-1; E,F: 24.5 GPa, exp. 2425, KLB-1 (the overview image of the double capsule is a secondary electron image).

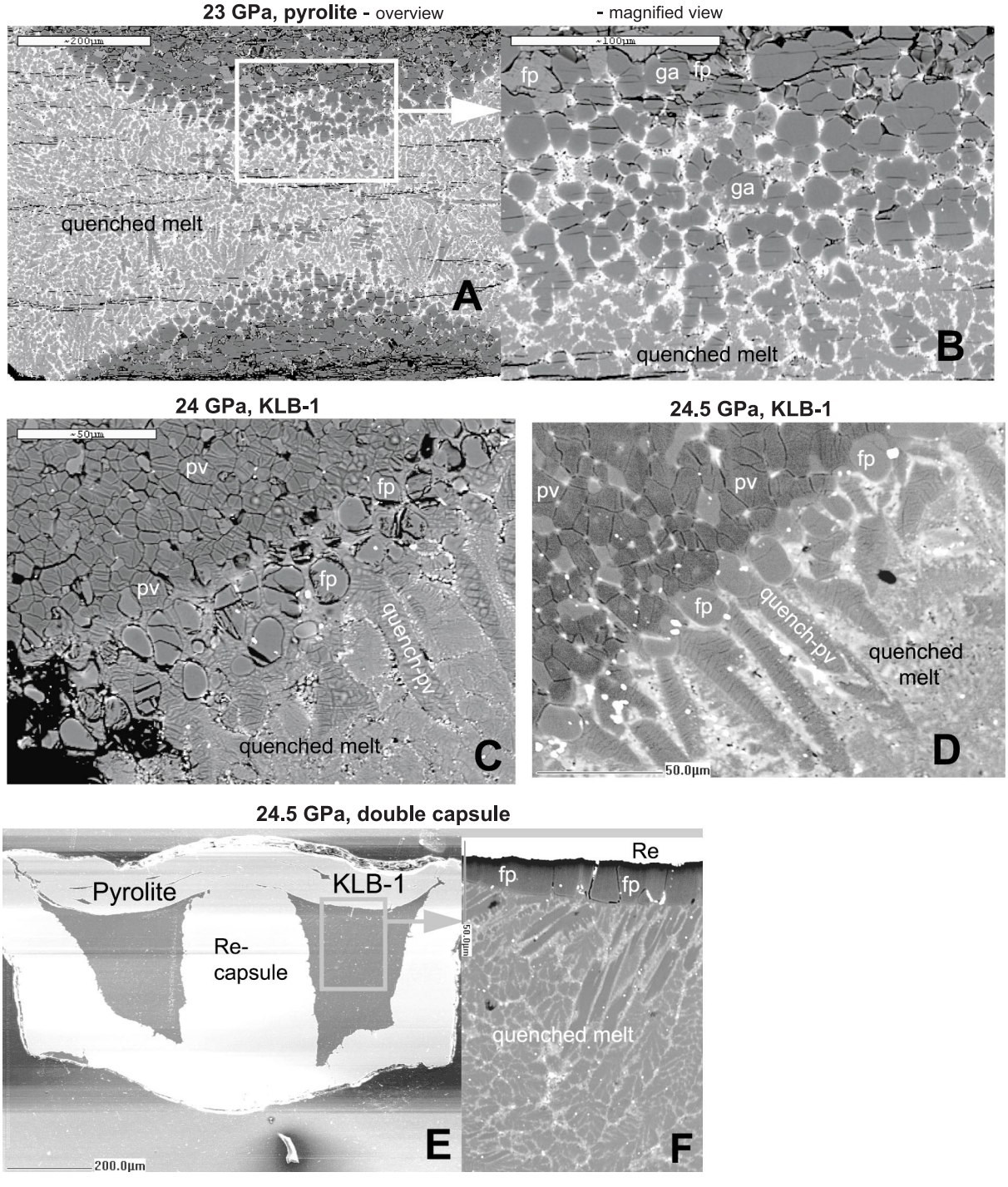
23 GPa, pyrolite - overview
- magnified view
~200µm
quenched melt
A
~100µm
fp
ga
fp
ga
quenched melt
B
24 GPa, KLB-1
~50µm
pv
fp
pv
fp
quench-pv
quenched melt
C
24.5 GPa, KLB-1
fp
pv
pv
fp
quench-pv
quenched melt
D
50.0µm
24.5 GPa, double capsule
Pyrolite
KLB-1
Re-
capsule
E
200.0µm
Re
fp
fp
950µm
quenched melt
F

to more interstitial melt, in the 18–8 mm assemblies (Fig. 2A,B), relative to the 10–4 mm assemblies. The crystallization sequence is inferred from the relative proximity of the different phases to the liquidus (see discussion in [8]). Three of the high-temperature run products from experiments at 24.5 GPa (Table 1, Fig. 2E) contain small amounts of ferropericlase as the only solid phase along the cold side of the sample capsules, documenting more clearly the liquidus phase at this pressure. Some of the experimental products, however, contain large and rather homogeneous quench crystals of garnet and perovskite growing from the liquidus boundary, into the liquid (Fig. 2C,D). The quenched garnet crystals in experiments 2383 and 2438 are 50–200 μm in size and occur as single and regularly zoned crystals (see analyses in **Background Data Set**[1]).

The addition of 1 wt% metallic iron to one of the 24 GPa experiments (2389) has an interesting effect on the phase relations. The resulting crystallization sequence is fp-pv-ga in contrast to the fp-ga-pv sequence observed in the other 24 GPa experiments. The stabilization of garnet relative to perovskite may be explained by the oxygen reducing effect of the addition of metallic Fe, suggesting that garnet is stabilized at more reducing conditions relative to perovskite. An ongoing experimental study carried out on a primitive mantle model composition at comparable conditions, but using diamond capsules, indicates that the crystallization of perovskite is suppressed relative to the other phases [20]. This may be explained by lower oxygen fugacity imposed by the diamond capsules (compared to Re capsules), even if the primitive mantle starting composition also has slightly higher contents of Si, Al, and Ca.

The phase relations of Fig. 1 are in broad agreement with the results of previous melting studies of KLB-1 up to 22.5 GPa [8,9], although there are minor differences. This study extends the phase relations to 24.5 GPa and documents more clearly that ferropericlase is the first liquidus phase of peridotite at pressures above 23 GPa. Although the liquidus temperature determined in our study is slightly lower than that previously determined for KLB-1 [8,9], our inferred solidus temperature is almost identical to that of previous measurements [8,27].

One of the discrepancies between previous melting studies of peridotite [8,9] and our results is the question of whether ringwoodite is present in the melting range and/or in the subsolidus assemblage at pressures of 22–23 GPa. Ringwoodite was found just above and below the solidus at about 22 GPa [9], but is absent from both the melting range and the subsolidus assemblages of all of our 22 and 23 GPa experiments. Even the 100% subsolidus experiments contain only the three-phase assemblage ga-fp-cpv at 22 GPa (experiment 2377) and the four-phase assemblage pv-ga-fp-cpv at 23 GPa (Z121).

Our results indicate that at high temperature (2000–2200°C) the perovskite-forming reaction is from majoritic garnet to perovskite as opposed to the ringwoodite to perovskite+ferropericlase reaction that occurs at lower temperatures. A recent experimental study of the subsolidus phase relations of the KLB-1 composition confirms the absence of ringwoodite near the solidus at pressures just below the perovskite-forming reaction [28]. The absence of subsolidus ringwoodite in our 22 GPa experiments is clearly not related to slow reaction rates during heating after the 20 min dwell periods at 1400°C, because the ringwoodite-out reaction boundary has a negative dp/dT slope (Fig. 1) [28].

4.2. Phase compositions

A range of mineral and melt compositions are shown in the major oxide variation diagrams in Fig. 3. Table 2 shows the average phase compositions, including normalized formula units, of minerals and melts at or slightly below the liquidus for the four different pressures. The compositions of coexisting minerals above and below the solidus are listed in the **Background Data Set**[1]. The melt composition of each run product is homogeneous throughout the quenched melt portions of the charges and similar to the bulk composition. The melt compositions are slightly enriched in Fe and Si and depleted in Mg, relative

[1] http://www.elsevier.com/locate/epsl

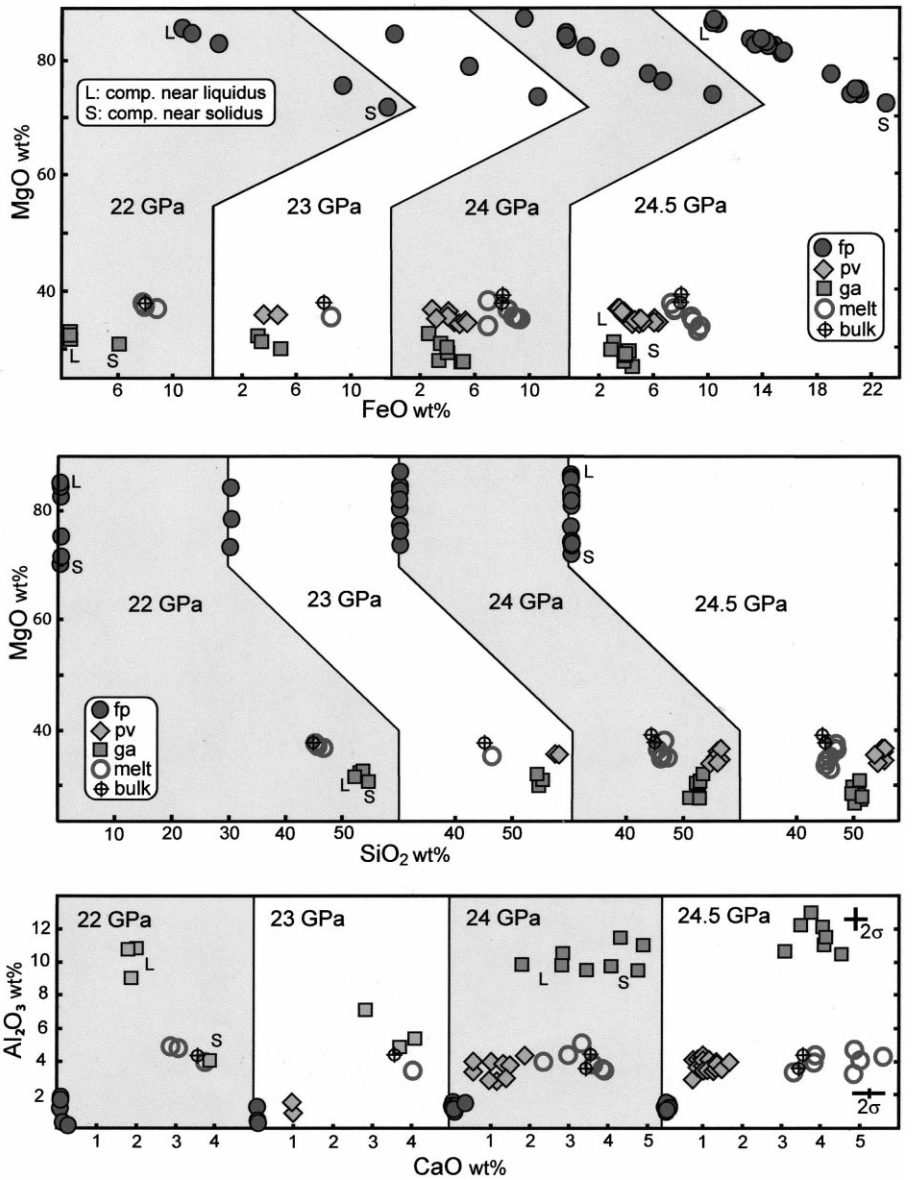

Fig. 3. Major oxide variation diagrams (wt%). Abbreviations as in Tables 1 and 2. The 2σ analytical error bars (Table 2) are within the symbols except for the error bars for CaO and Al_2O_3 for quenched melt and garnet, which are shown (2σ) on the right panel.

to the bulk composition (Fig. 3). Generally, tie lines (not shown in the variation diagrams) between the two first crystallizing phases and the melt compositions form triangles that enclose the bulk compositions. Corresponding tie lines between the subsolidus compositions must include CaSi-perovskite, which is not included in the diagrams. The most noticeable change in mineral chemistry when going from liquidus to solidus is the strong increase in the Fe/Mg ratio. This change, observed in several other experimental melting studies (e.g. [9,11]), is seen in all of the minerals but is most pronounced in ferropericlase (Fig. 3).

The liquidus ferropericlase has a remarkably constant composition within the 22–24.5 GPa pressure range, with an Mg number [100*Mg/(Mg+total Fe)] of 92.3 ± 0.3 (Table 2). This rather high Mg number is slightly lower than the liquidus perovskites (94.3 ± 0.2) and garnet (94.9 ± 0.8). The Mg numbers in these minerals do not seem to vary systematically with pressure. The Mg numbers, however, decrease markedly as a function of the distance from the liquidus.

The majorite component of the liquidus garnet increases from 61.4 mol% at 22 GPa to 71.7 mol% at 23 GPa, but decreases again to 61.5% at 24 GPa, due to the appearance of coexisting perovskite. The cation sums of the garnet are within 0.2% of the expected eight cations, when normalized to a cation charge of 24 (12 oxygen atoms). The perovskite formulas, on the other hand, are characterized by small, but consistent cation excesses of 0.03–0.08 (0.4–1%) relative to the expected eight cations per formula unit of 12 O atoms. Perovskites with considerably larger cation excesses of 0.11–0.16 (1.4–2%) were observed in a similar study of a more Fe-rich composition [11]. Several studies [26,31,32] indicate that aluminous magnesium silicate perovskite has a strong affinity for ferric iron. If the entire cation excess of 0.034–0.076 in the formulas normalized to 12 oxygen atoms (liquidus perovskites at 24 and 24.5 GPa, Table 2) is ascribed to the presence of ferric iron, the charge balance of a formula normalized to 8.00 cations requires a Fe^{3+}/Fe_{total} ratio of 0.5–1. Similar magnitude Fe^{3+}/Fe_{total} ratios were measured by energy-loss near-edge structure spectrometry in aluminous perovskites equilibrated with ferropericlase and garnet in Re capsules at 24–26 GPa and 1650–1900°C (Frost and Langenhorst, submitted). The apparent cation excess may alternatively be ascribed to an aluminous- and oxygen-deficient perovskite [33]. Only 5–10% of the oxygen-deficient component $Mg_4Al_2Si_2O_{11}$ would be required to account for the apparent cation excess.

Some of the majoritic garnet crystals have significant compositional zoning. For grains located relatively close to the liquidus the zoning involves cores with higher Fe/Mg ratios than the rims. Such Fe-rich cores represent incompletely equilibrated crystals that formed during heating towards the run temperature. Care was taken to obtain the rim composition of such grains. Similar compositional heterogeneities were not observed in perovskite and ferropericlase. The larger analytical uncertainties for garnet than for perovskite and ferropericlase (Table 2) may largely reflect these compositional heterogeneities.

The crystals of CaSi-perovskite are often too small for electron microprobe analyses. It seems that the presence of 0.45% trace element oxides in the pyrolite starting composition enhances the crystal growth. Therefore all of the analyses (**Background Data Set**[1]) of this phase are from trace element-doped pyrolite bulk compositions. The analyzed CaSi-perovskites have major oxide totals of about 88 wt%, implying the presence of about 12 wt% trace elements.

4.3. Hydrogen and ferric iron

One of the 24 GPa run products (2387) was made into a doubly polished thin section for an exploratory investigation by FTIR and Mössbauer spectroscopy. Hydroxyl was not detected at an estimated detection level of 100 ppm. Although we found no evidence for hydrogen in the crystals of the solid assemblage or quenched liquid, we cannot exclude the possibility that water in the liquid may have been quenched to a free fluid phase and thereby escaped detection.

The Fe^{3+}/Fe_{total} ratio was found to be 0.19 in the quenched melt and 0.28 in the bulk crystal aggregate. Although the iron in the starting material was reduced to ferrous iron in a gas mixing furnace, there are relatively large reservoirs of oxygen in the form of ceramic oxides in the pressure cell parts surrounding the sample capsules. Before compression these ceramic parts, as well as the sample powder itself, also contain oxygen in their pore space volumes. The ceramic parts, in particular, contain considerable pore space. It is likely that a small amount of ferrous Fe from the sample converted to metallic Fe that alloyed with the inner walls of the Re capsules during the experiments, causing some oxidation of the sample. Previous experiments in a more Fe-rich composition [11] have shown that the innermost walls of

the Re capsules can contain up to 1 wt% Fe. Due to the procedures to remove H_2O from the sample surroundings before the experiments, it is unlikely that there was any significant water present in the samples. If, however, some water was present, oxidation of the sample could conceivably occur by dissociation of H_2O in combination with diffusive H loss.

It is interesting to note that the proportion of ferric Fe is higher in the bulk crystal aggregate than in the quenched melt. The reason for such a preferential partitioning is most likely that Al-bearing perovskite has greater affinity for Fe^{3+} than the other phases, including the quenched melt phase (see the discussion above).

5. Mineral–melt partitioning

5.1. Major elements

Fig. 4 summarizes the mineral–melt partitioning of major and minor elements from our study and includes some of the data from Herzberg and Zhang [9]. There is a good agreement between our determined partitioning ratios and those reported by [9]. In Fig. 4 the mineral–melt partitioning of major elements is shown as exchange distribution ratios, labelled K_D, involving the Si/Mg, Fe/Mg and Ca/Al ratios. These K_D values $[=(i/j)_{mineral}/(i/j)_{melt}]$ do not correspond to chemical equilibrium constants for simple ionic exchange reactions between solid and liquid, and are therefore not strictly equivalent to true exchange distribution coefficients [34]. This applies even to the Fe/Mg ratio, because of the complex Fe partitioning in perovskite (e.g. [32]). Hanson and Langmuir [35] classified these elements as essential structural constituents (ESC: Si, Al, Ca) and intermediate elements (Mg, Fe^{2+}), respectively. The ratios of true ESC elements are constant for a given mineral, and a variation of exchange distribution coefficients for ESCs will therefore reflect the variation in melt composition. The increasing solubility of the majorite ($(Mg,Fe)SiO_3$) component in garnet with increasing pressure, however, implies that Si, Al and Ca cannot be considered true ESC elements in this phase.

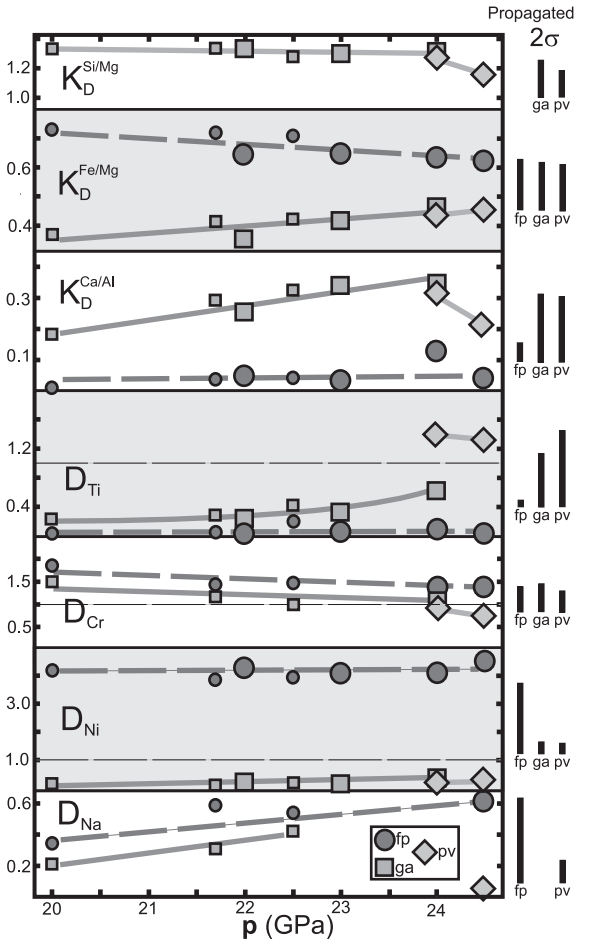

Fig. 4. Mineral–melt partitioning ratios for major and minor elements. Symbol shapes as in Fig. 3, small symbols from Herzberg and Zhang [9] and large symbols from this investigation. The K_D ratios are not true partitioning coefficients linked to equilibrium constants of simple cation mineral–melt exchange reactions (further discussion in the text). The D_{Cr} values derived from our data set are based on only the experiments with KLB-1 starting material. $K_D^{i/j}=(i/j)_{mineral}/(i/j)_{melt}$; $D_i=(i)_{mineral}/(i)_{melt}$. The propagated 2σ error bars, shown to the right of each of the panels, are calculated from the average analytical errors in Table 2.

At lower pressures the mineral–melt K_D(Fe/Mg) is largely independent of composition and temperature, because of the geochemical similarity between these two elements and because the compositional effects on the D_i (Nernst distribution coefficient) for Fe and Mg cancel out [9]. Such a simple Fe–Mg relationship does not exist for perovskite, however, due to the preferential

incorporation of significant amounts of ferric iron in a coupled substitution with Al. In Fig. 4 the Fe/Mg ratio involves the sum of ferric and ferrous Fe, even if Fe^{3+} is partitioned selectively into the bulk mineral assemblage relative to the liquid, and into the perovskite relative to garnet and ferropericlase.

The K_D(Si/Mg) for garnet remains almost constant at 1.3 in the 20–24 GPa range, whereas the corresponding value for perovskite is slightly lower (1.2) and shows a decreasing trend from 24 to 24.5 GPa. The K_D(Fe/Mg) remains well below unity for all of the minerals. With increasing pressure from 20 to 25 GPa, an increase from below 0.4 towards 0.5 for garnet and perovskite is opposed by a decrease from 0.7 to 0.6 for ferropericlase. The increase in the Fe/Mg ratio of the melt relative to the bulk solid residue is accompanied by an even stronger increase in the Ca/Al ratio of the melt. The K_D(Ca/Al) is well below 0.4 for all of the minerals. With increasing pressure, the K_D(Ca/Al) increases for garnet and decreases for perovskite. The major element partitioning coefficients derived for the investigated peridotite compositions overlap with corresponding coefficients for a composition with much higher Fe/Mg ratio [11], indicating that the K_D values are rather insensitive to moderate variations in bulk composition.

5.2. Minor elements

The mineral–melt partitioning of the minor elements, Ti, Cr, Ni, and Na, is shown by the simple Nernst distribution coefficients in Fig. 4. Ti is compatible in perovskite ($D_{Ti} = 1.3–1.4$) and incompatible in garnet and ferropericlase ($D_{Ti} < 0.1$). The D_{Ti} value for garnet increases from 0.2 to 0.6 with increasing pressure. The behavior of chromium is inverse to that of Ti, with D_{Cr}(garnet) decreasing from 1.5 to 1.1 and D_{Cr}(ferropericlase) decreasing from 1.8 to 1.4 with increasing pressure. Cr is weakly incompatible in perovskite. Nickel is strongly compatible in ferropericlase and incompatible in garnet and perovskite, with partitioning coefficients of 4.0–4.3 and 0.2–0.4, respectively. There is no discernible variation in the Ni partitioning as a function of pressure. Sodium is incompatible in all of the solid phases. The compatibility in both garnet and ferropericlase, however, seems to increase as a function of pressure, and the D_{Na} value for ferropericlase reaches 0.6 at 24.5 GPa.

It is interesting to note that the weak pressure-dependent trends for garnet–melt partitioning of Ti, Cr and Na observed in Fig. 4 are largely in accordance with the garnet–melt partitioning at 15 GPa [12]. Various other studies of garnet–melt and perovskite–melt partitioning, however, show somewhat different behavior for some of these elements. Whereas Drake et al. [36] and McFarlane et al. [43] report D_{Cr}(garnet) values of 1.0 to 1.5, which are broadly in agreement with our results, Ohtani et al. [37] derived a higher value of 2.3. The D_{Ti}(perovskite) values and D_{Cr}(perovskite) values of [13,14,36,38–41] have wide ranges of 0.6–3.0 and 0.4–6.3, respectively. The values of McFarlane et al. [13], however, are in overall agreement with the present results. There are considerable differences in major element bulk composition between the calcic ultrabasic system of [14,40] and the peridotitic composition of the present study. The Ni partitioning perovskite–melt and ferropericlase–melt, however, does not show large variations between the various studies, and the ferropericlase–melt partitioning of Ti and Cr is generally also consistent between the studies.

The recent development of improved microanalytical techniques for trace element analyses (laser ablation ICPMS and SIMS) makes it possible to acquire a large range of elemental mineral–melt partitioning data. The design and performance of stable equilibrium experiments at pressures above 20 GPa now represent the main challenge in generating high-quality partitioning data for minor and trace elements between majoritic garnet, ferropericlase, perovskite and ultramafic silicate melts.

6. Implications for early mantle differentiation

The liquidus phase relations of common peridotite compositions derived in this study demonstrate clearly that ferropericlase is on the perido-

tite liquidus above about 23.2 GPa. This was not recognized in some of the early melting studies of peridotitic and chondritic composition in this pressure range (e.g. [7,42]). Later, studies (e.g. [8,10,11,43]), however, have observed ferropericlase on or near the liquidus in peridotitic and chondritic compositions at pressures corresponding to the transition zone and the lower mantle. In this study, three of the high-temperature run products from experiments at 24 GPa contain small amounts of ferropericlase as the only solid phase along the cold end of the sample capsules, demonstrating clearly that ferropericlase is the first liquidus phase. Although ferropericlase is the liquidus phase in the 23–25 GPa range, ongoing melting studies, using multianvil configurations with sintered diamond anvils, indicate that perovskite becomes the first liquidus phase above 31 GPa [44]. At 33 GPa Ca-perovskite also crystallizes closer to the liquidus and almost simultaneously with ferropericlase.

Another important observation from this investigation is the absence of ringwoodite in the high-temperature part of the subsolidus region at pressures just below the perovskite-forming reaction boundary. This implies that the high-temperature perovskite-in transition has a positive dp/dT slope [28] and that hot plumes ascending from the lower mantle will be accelerated rather than delayed at the bottom of the mantle transition zone.

An implication of the early crystallization of ferropericlase from melts in the lower part of the transition zone and the uppermost part of the lower mantle is that the proposed mechanism of producing a lower mantle with an elevated Si/Mg ratio relative to the upper mantle and chondritic compositions by fractionation of perovskite [45] may not be a viable process. Because the observed K_D(Si/Mg) for perovskite is close to unity (1.2), the addition of even small amounts of ferropericlase to the crystallizing assemblage would decrease rather than increase the Si/Mg ratio in bulk solid material. At depths exceeding 850 km, however, the possibility of perovskite-dominated fractionation [44] may facilitate the production of residues with elevated Si/Mg ratios relative to a bulk silicate Earth composition. The additional possibility of near-liquidus coprecipitation of Mg- and Ca-perovskites may further enhance the residual Si/Mg ratio, as well as the REE and HFSE concentrations in the residue or fractionated assemblage.

The density relations between coexisting perovskite, ferropericlase and melt at 500–800 km depth in the Earth [11,45,46] indicate that partial melts will be buoyant relative to these minerals, and that fractionation of ferropericlase and perovskite from rising melt fractions, either in a solidifying magma ocean or from subsequent hot plumes, can be expected to occur. Strong convective motions during magma ocean crystallization, however, may largely have erased the memory of such a fractionation [2].

The partitioning relations shown in Fig. 4 indicate that fractional crystallization or partial melting in the transition zone and the upper part of the lower mantle would increase the Fe/Mg and Ca/Al ratios and the Na concentration of the melt. Whereas the K_D(Fe/Mg) for ferropericlase–melt partitioning is always lower than 0.7 in our measurements and is observed to decrease with pressure towards lower mantle conditions, previous studies [47,48] have found above-unity values for this partitioning. Such discrepancies may result from the measurement of subliquidus ferropericlase compositions in extreme thermal gradients [11].

The mineral–melt partitioning of Ti and other high field strength elements is strongly dependent on whether perovskite is part of the residual or fractionating assemblage. The high field strength elements are compatible in perovskite, but incompatible in garnet and ferropericlase. Cr partitioning is generally opposite to that of Ti, although the D_{Cr} for all of these phases cluster closer to unity than the D_{Ti}.

Acknowledgements

The high-pressure experiments were performed at the Bayerisches Geoinstitut under the EU-TMR Large Scale Facilities program (Contract No. ERBFMGECT980111 to D.C. Rubie). A part of the analytical work carried out at the University of Bristol was supported by a contract

under the EU-IHP program (Access to Research Infrastructures) to B.J. Wood. C.A. McCammon kindly performed the reconnaissance Mössbauer spectroscopy analyses. Further analytical assistance was provided by J.A. Dalton, M. Erambert, S. Kears, J. Sowerby and T. Winje. Discussions with K. Hirose, E. Ito, E. Takahashi and M.J. Walter, journal reviews by C. Herzberg and E. Takahashi, and editorial handling by B.J. Wood are greatly appreciated.*[BW]*

References

[1] G.W. Wetherill, Formation of the Earth, Annu. Rev. Earth Planet. Sci. 18 (1990) 205–256.
[2] W.B. Tonks, H.J. Melosh, The physics of crystal settling and suspension in a turbulent magma ocean, in: N.E. Newsom, J.H. Jones (Eds.), Origin of the Earth, Oxford University Press, New York (1990) 151–174.
[3] Q. Xie, R. Kerrich, Silicate-perovskite and majorite signature komatiites from the Archean Abitibi greenstone belt: Implication for early mantle differentiation and stratification, J. Geophys. Res. 99 (1994) 15799–15812.
[4] C.T. Herzberg, Generation of plume magmas through time: an experimental perspective, Chem. Geol. 126 (1995) 1–18.
[5] C.B. Agee, D. Walker, Comments on 'Constraints on element partition coefficients between $MgSiO_3$ perovskite and liquid determined by direct measurements' by Kato, T., Ringwood, A.E., Irifune, T., Earth Planet. Sci. Lett. 94 (1989) 160–161.
[6] T. Kato, A.E. Ringwood, T. Irifune, Constraints on element partition coefficients between $MgSiO_3$ perovskite and liquid determined by direct measurements. Reply to C.B. Agee and D. Walker, Earth Planet. Sci. Lett. 94 (1989) 162–164.
[7] E. Ito, E. Takahashi, Melting of peridotite at uppermost lower mantle conditions, Nature 328 (1987) 514–517.
[8] J. Zhang, C. Herzberg, Melting experiments on anhydrous peridotite KLB-1 from 5.0 to 22.5 GPa, J. Geophys. Res. 99 (1994) 17729–17742.
[9] C.T. Herzberg, J. Zhang, Melting experiments on anhydrous KLB-1: compositions of magmas in the upper mantle and transition zone, J. Geophys. Res. 101 (1996) 8271–8295.
[10] C.B. Agee, J. Li, M.C. Shannon, S. Circone, Pressure-temperature phase diagram for the Allende meteorite, J. Geophys. Res. 100 (1995) 17725–17740.
[11] R.G. Trønnes, Melting relations and major element partitioning in an oxidized bulk Earth model composition at 15–26 GPa, Lithos 53 (2000) 233–245.
[12] T. Suzuki, M. Akaogi, E. Nakamura, Partitioning of major elements between garnet-structured minerals and silicate melt at pressure of 3–15 GPa, Phys. Earth Planet. Inter. 120 (2000) 79–92.
[13] E.A. McFarlane, M.J. Drake, D.C. Rubie, Element partitioning between Mg-perovskite, magnesiowüstite and silicate melt at conditions of the earths mantle, Geochim. Cosmochim. Acta 58 (1994) 5161–5172.
[14] H. Taura, H. Yurimoto, T. Kato, S. Sueno, Trace element partitioning between silicate perovskites and ultracalcic melt, Phys. Earth Planet. Inter. 124 (2001) 25–32.
[15] M. Akaogi, E. Ito, A. Navrotsky, Olivine-modified spinel-spinel transitions in the system Mg_2SiO_4-Fe_2SiO_4: calorimetric measurements, thermochemical calculation and geophysical application, J. Geophys. Res. 94 (1989) 15671–15685.
[16] S. Ono, T. Katsura, E. Ito, M. Kanzaki, A. Yoneda, M.J. Walter, S. Urakawa, W. Utsumi, K. Funakoshi, In situ observation of ilmenite-perovskite phase transition using synchrotron radiation, Geophys. Res. Lett. 28 (2001) 835–838.
[17] J.C. Jamieson, J.N. Fritz, M.H. Manghnani, Pressure measurement at high temperature in x-ray diffraction studies: gold as a primary standard, in: S. Akimoto, M.H. Manghnani (Eds.), High-Pressure Research in Geophysics, CAP, Tokyo, 1982, pp. 27–48.
[18] Y. Fei, C.M. Bertka, Phase transitions in the Earth's mantle and mantle mineralogy, in: Y. Fei, C.M. Bertka, B.O. Mysen (Eds.), Mantle Petrology: Field Observations and High-Pressure Experimentation: A Tribute to Francis R. (Joe) Boyd, Geochem. Soc. Spec. Publ. 6 (1999) 189–207.
[19] R.G. Trønnes, D.J. Frost, Liquidus phase relations and major element partitioning in peridotite at 21–24 GPa, EOS Trans. Am. Geophys. Union 81 (2000) F1297.
[20] R.G. Trønnes, D.J. Frost, M.J. Walter, C. McCammon, E. Nakamura, Phase relations of peridotite at 21–24 GPa and variable oxygen fugacity: implications for the 660 km discontinuity, EOS Trans. Am. Geophys. Union 82 (2001) F900.
[21] T. Irifune, N. Nishiyama, K. Kuroda, T. Inoue, M. Isshiki, W. Utsumi, K. Funakoshi, S. Urakawa, T. Uchida, T. Katsura, O. Ohtaka, The postspinel phase boundary in Mg_2SiO_4 determined by in situ X-ray diffraction, Science 279 (1998) 1698–1700.
[22] K. Hirose, Y. Fei, S. Ono, T. Yagi, K. Funakoshi, In situ measurements of the phase transition in $Mg_3Al_2Si_3O_{12}$: implications for the nature of the seismic discontinuities in the Earth's mantle, Earth Planet. Sci. Lett. 184 (2001) 567–573.
[23] O.L. Anderson, D.G. Isaak, S. Yamamoto, Anharmonocity and the equation of state of gold, J. Appl. Phys. 65 (1989) 15663–15670.
[24] S.-H. Shim, T.S. Duffy, G. Shen, The post-spinel transition in Mg_2SiO_4 and its relation to the 660-km seismic discontinuity, Nature 411 (2001) 571–574.
[25] L. Chudinovskikh, R. Bohler, High-pressure polymorphs of olivine and the 660-km seismic discontinuity, Nature 411 (2001) 574–577.

[26] B.J. Wood, Phase transformations and partitioning relations in peridotite under lower mantle conditions, Earth Planet. Sci. Lett. 174 (2000) 341–351.
[27] C. Herzberg, P. Raterron, J. Zhang, New experimental observations on the anhydrous solidus for peridotite KLB-1, Geochem. Geophys. Geosyst. 1 (2000) 2000GC000089.
[28] K. Hirose, Phase transitions in pyrolitic mantle around 670-km depth: implications for upwelling of plumes from the lower mantle, J. Geophys. Res., in press.
[29] W.F. McDonough, S.-s. Sun, The composition of the Earth, Chem. Geol. 120 (1995) 223–253.
[30] E. Takahashi, Melting of dry peridotite up to 14 GPa: Implications on the origin of peridotitic upper mantle, J. Geophys. Res. 91 (1986) 9367–9382.
[31] C. McCammon, Perovskite as a possible sink of ferric iron in the lower mantle, Nature 387 (1997) 694–696.
[32] B.J. Wood, D.C. Rubie, The effect of alumina on phase transformations at the 660-kilometer discontinuity from Fe-Mg partitioning experiments, Science 273 (1996) 1522–1524.
[33] J.D. FitzGerald, A.E. Ringwood, High-pressure rhombohedral perovskite phase $Ca_2AlSiO_{5.5}$, Phys. Chem. Minerals 18 (1991) 40–46.
[34] S. Banno, Y. Matsui, On the formulation of partition coefficients for trace elements distribution between minerals and magma, Chem. Geol. 11 (1973) 1–15.
[35] G.N. Hanson, C.H. Langmuir, Modelling of major elements in mantle-melt systems using trace element approaches, Geochim. Cosmochim. Acta 42 (1978) 725–741.
[36] M.J. Drake, E.A. McFarlane, T. Gasparik, D.C. Rubie, Mg-perovskite/silicate melt and majorite garnet/silicate melt partition coefficients in the system CaO-MgO-SiO_2 at high temperatures and pressures, J. Geophys. Res. 98 (1993) 5427–5431.
[37] E. Ohtani, I. Kawabe, J. Moriyama, Y. Nagata, Partitioning of elements between majorite garnet and melt and implications for the petrogenesis of komatiites, Contrib. Mineral. Petrol. 103 (1989) 263–269.
[38] T. Kato, A.E. Ringwood, T. Irifune, Constraints on element partitioning coefficients between $MgSiO_3$ perovskite and liquid by direct determination, Earth Planet. Sci. Lett. 90 (1988) 65–68.
[39] T. Kato, A.E. Ringwood, T. Irifune, Experimental determination of element partitioning between silicate perovskites, garnets and liquids: constraints on early differentiation of the mantle, Earth Planet. Sci. Lett. 89 (1988) 123–145.
[40] T. Kato, E. Ohtani, Y. Ito, K. Onuma, Element partitioning between silicate perovskites and calcic ultrabasic, Phys. Earth Planet. Inter. 96 (1996) 201–207.
[41] E. Ohtani, T. Kato, E. Ito, Transition metal partitioning between lower mantle and core materials at 27 GPa, Geophys. Res. Lett. 18 (1991) 85–88.
[42] E. Ohtani, H. Sawamoto, Melting experiment on a model chondritic mantle composition at 25 GPa, Geophys. Res. Lett. 14 (1987) 733–736.
[43] E.A. McFarlane, M.J. Drake, C.T. Herzberg, Ferropericlase/melt and majorite/melt partitioning and the early thermal history of the Earth, Proc. Lunar Planet. Sci. Conf. 22 (1991) 875–876.
[44] M.J. Walter, E. Ito, E. Nakamura, R.G. Trønnes, D. Frost, New experimental constraints on crystallization differentiation in a deep magma ocean, EOS Trans. Am. Geophys. Union 82 (2001) F27.
[45] C.B. Agee, D. Walker, Mass balance and phase density constraints on the early differentiation of chondritic mantle, Earth Planet. Sci. Lett. 90 (1988) 144–156.
[46] C.B. Agee, Crystal-liquid density inversions in terrestrial and lunar magmas, Phys. Earth Planet. Inter. 107 (1998) 63–74.
[47] C.B. Agee, A new look at differentiation of the Earth from melting experiments on the Allende meteorite, Nature 346 (1990) 834–837.
[48] C.B. Agee, High-pressure melting of carbonaceous chondrite, J. Geophys. Res. 98 (1993) 5419–5426.